JOM
https://doi.org/10.1007/s11837-023-06167-w

ADDITIVE MANUFACTURING FOR HIGH TEMPERATURE ENERGY SYSTEMS: HARVESTING MATERIAL DATA AND MODELING

Reactive Synthesis in Additive Manufacturing of an Ultrahigh Temperature MoSiB Alloy

ZAHABUL ISLAM,[1,2] MARSHAL AMALRAJ,[3] LONGFEI LIU,[2] LAURENCE D. MARKS,[3] JOHN H. PEREPEZKO,[2] and DAN J. THOMA [2,4]

1.—Mechanical and Manufacturing Engineering Program, School of Engineering Technology, Bowling Green State University, Bowling Green, OH 43403, USA. 2.—Department of Materials Science and Engineering, University of Wisconsin, Madison, WI 53706, USA. 3.—Department of Materials Science and Engineering, Northwestern University, Evanston, IL 60208, USA. 4.—e-mail: dthoma@wisc.edu

To address the challenges of processing ultrahigh-temperature refractory metal alloys, a novel reactive synthesis-based additive manufacturing technique has been developed to fabricate chemically uniform and dense alloys. The present study demonstrates the reactive additive manufacturing of Mo-4Si-6B (at.%), a high-temperature refractory alloy, using directed energy deposition. For the alloy in the Mo-Si-B system, a premixed blend of molybdenum, silicon nitride, and boron nitride powder was used to make an alloy with the desired composition. A dimensionless number was used to design the process parameters and build efficiency. High-throughput synthesis using build height measurements of individual samples validated the predicted process parameters. Microstructural characterization investigations and indentation hardness testing indicated chemically uniform samples with refined microsegregation in samples with high hardness and no cracking, even with a 10-kg force load. The results demonstrate an effective strategy for additively manufacturing refractory alloys.

INTRODUCTION

Among the several potential refractory metal alloy candidates, Mo-based alloys have a wide range of applications, including but not limited to aerospace, nuclear energy, and chemical processing.[1–4] Mo-based alloys offer excellent high-temperature mechanical properties as well as thermal stability, due to their high melting points,[5–7] low thermal expansion coefficient, high thermal conductivity, and good fatigue resistance.[8,9] Mo-based alloys also offer lower density compared to tantalum and tungsten, which is favorable for the aerospace industry where weight is a primary concern. Among the Mo-based alloys, the Mo-Si-B system has received attention due to the very high melting point and oxidation resistance of the alloys.[10,11] The performance of three-phase Mo_{ss} + Mo_3Si + T2 alloys is related to the BCC α-Mo phase that provides ductility, the silicide phases that enable high-temperature creep resistance, and by the Mo_5SiB_2 (T2) phase that, in addition to high-temperature strength, facilitates the formation of a borosilicate glass to protect against oxidation. However, the α-Mo phase has Si dissolved within the solid solution, and the dissolved Si has been known to cause a high level of work hardening at room temperature, leading to brittle fracture.[12,13] Thus, a reduction in the Si content in Mo_{ss} can improve the low-temperature ductility of Mo-Si-B alloys.[14–17]

Conventional powder metallurgy processing approaches for refractory metal alloys (RMAs) involve several steps including the hot-pressing of RMA powders, high-temperature sintering, and then usually a hot isostatic press treatment to achieve full density.[10,18] Even with these multiple processing steps for net-shape products, it is difficult to produce complex shapes with accurate geometric control. Likewise, conventional casting, such as in the superalloy turbine industry,

(Received May 31, 2023; accepted September 21, 2023)

Published online: 23 October 2023

introduces ceramic mold containment issues for net-shape processing because of the high temperatures. As a potential alternative, additive manufacturing (AM) permits the focused melting of refractory metal net shapes without the containment challenges or sintering requirements of casting or powder metallurgy processing techniques. With AM methods such as directed energy deposition (DED), alloying is accomplished by melting thin layers of powder mixtures to full density. Tight tolerances and control can also be achieved, as well as complex internal features for cooling.[19]

The present study aims to develop the processing parameters for a viable, ultrahigh-temperature alloy using metal AM to manufacture dimensionally controlled shapes in a commercially cost-effective way. To accomplish this goal, a DED LENS system has been used to print Mo-Si-B alloys. In addition, the approach includes using a reactive synthesis from the exothermic reaction of pure Mo, BN, and Si_3N_4 powder streams. The preliminary alloy compositions, in this case, 90 at.% Mo, 4 at.% Si, and 6 at.% B, were chosen based on a recent microstructural design that yields improved ductility and toughness.[17] For the successful printing of bulk samples, a dimensionless number-based methodology was used to predict the process parameters.[20] A combined high-throughput synthesis and microstructural characterization technique have validated the optimum process window for the efficient printing of the Mo-Si-B alloy.

MATERIALS AND METHODS

Directed Energy Deposition (DED) of Mo-Si-B Alloy

An Optomec LENS MR-7 (DED) was used to manufacture the Mo-Si-B ultrahigh-temperature refractory alloys. Near-spherical gas-atomized molybdenum (Mo), Si_3N_4, and BN (shown in Fig. 1a–c) were premixed. Changes in pre-alloyed, refractory powder compositions can be expensive, and the blending of commercially available constitutive powder can lower the cost and increase the compositional alloy design flexibility, provided that homogeneous samples can be produced. To assist in the ability to supply adequate heat for both processing and homogenization, reactive synthesis was introduced into the DED processing. A molten puddle was maintained by the intersection of the blended powder stream and the laser heat source. The reaction of Mo with Si_3N_4 and BN produced the following, exothermic reaction:[21]

$$5Mo + 1/3Si_3N_4 + 2BN \rightarrow Mo_5SiB_2 + 5/3N_2 \quad (1)$$

The formation enthalpy of Mo_5SiB_2 is -199.7 kJ/mol.[22] The premixed powder was loaded into one of the four hoppers connected to the LENS MR-7. An argon carrier gas delivered the powders from the hoppers to the nozzle head of the DED system. A 1-kW Nd:YAG 1070-nm wavelength laser with a 600-μm spot size was used to melt the powder on a titanium build plate. The processing glove box had an Ar environment with an oxygen content of less than 10 ppm. The mass flow rate of the powder was calibrated and controlled by regulating the revolutions per minute of the auger attached to the hopper. A previously developed dimensionless number and relationship was used to define process parameters, namely, laser power (P), feed rate (v), powder mass flow rate ($\dot{m}$), laser hatch spacing (h), and layer thickness (Z), to analyze the variation in build heights.[20] The dimensionless number relationship was originally evaluated for Fe-based materials, but was evaluated for the Mo-Si-B system in this study.

A bi-directional, single-pass laser beam was used to build the samples, and a 0°–90° rotation of scan vectors was deployed for all the printings. Each sample was printed with an X–Y dimension of 6.3 mm × 6.3 mm. The distance between the build plate and the nozzle head, which is also known as the stand-off distance, was set to 9.53 mm. After completion of the printing of 25 samples, the build plate was taken out of the build chamber and the height of each individual sample was measured. The measured build height with respect to the dimensionless number was captured as a part of the high-throughput experiment. The synthesis is considered high-throughput since 25 samples can be generated in an afternoon as compared to arc-casting, where generally one sample can be produced in the same period.

The nominal alloy composition of the blended powder was Mo-4Si-6B (at.%), and the alloy composition is shown in the ternary diagram of Fig. 2.[23] Based upon this equilibrium diagram, the composition lies just inside the three-phase field of Mo_{ss} +

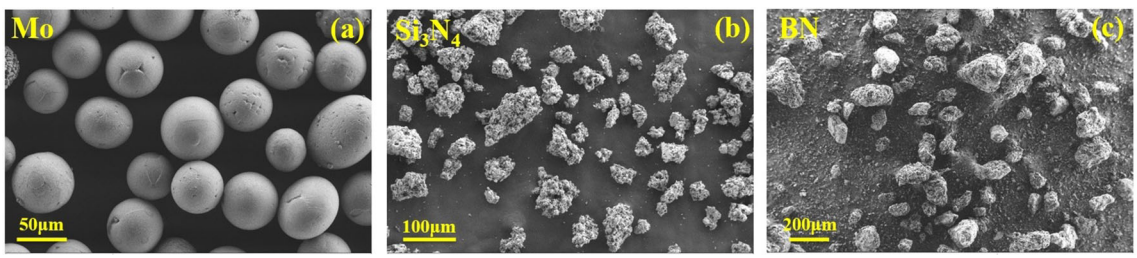

Fig. 1. Alloying powder: (a) molybdenum (Mo), (b) silicon nitride (Si_3N_4), (c) boron nitride (BN).

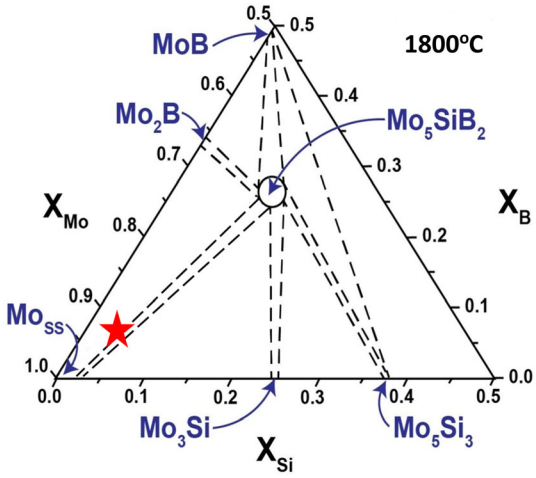

Fig. 2. Isothermal section of the Mo-Si-B phase diagram.

Mo_2B + T2 along the Mo_{ss} + T2 two-phase field at 1800°C. In the Mo-rich corner of the ternary diagram, the Si solid solubility limits in the Mo_{ss} + Mo_2B + T2 phase field are 1.38 at.% at 1600°C and 1.75 at.% Si at 1800°C, which is lower than the Si solubility limits in the Mo_{ss} phase in the Mo_{ss} + Mo_3Si + T_2 three-phase region.[23] A compositional shift towards the reduced solubility of Si in the Mo_{ss} is intended to provide more ductility in an alloy.

Microstructural Investigation

To investigate the microstructure, five test specimens at different dimensionless numbers were cold-mounted using epoxy resin to validate the process window. The mounted samples were polished using a diamond slurry with reducing particle sizes of 6 μm, 3 μm, and 1 μm, and with 50-nm colloidal silica, respectively. Following polishing, the samples were thoroughly cleaned with isopropanol and ethanol followed by deionized water. After cleaning the specimens, a scanning electron microscope (SEM) was used to investigate the microstructures in the as-printed samples. High-magnification SEM micrographs were captured using a ZEISS LEO 1530 equipped with a field-emission gun.

Atom Probe Tomography (APT)

An FEI Helios Nanolab SEM-FIB (focused ion beam) dual beam microscope, equipped with an Omniprobe AutoProbe 200 and Pt gas injection system was used for the site-specific lift-out and preparation of nano-tip samples for atom probe tomography (APT). A standard lift-out procedure was used on the AM sample, where the lifted-out sample was mounted on flat Si-posts via the manipulator needle and Pt welding. The nano-tips for APT were prepared by sequential annular milling using Ga ions at 30 kV, followed by a final 5-kV clean-up milling to minimize Ga ion implantation and high-voltage milling artifacts. The final APT tip had a tip diameter and shank angle of $\sim$ 25 nm and 30°, respectively. Near-atomic-scale 3D elemental distribution of the printed samples was visualized using a local electrode atom-probe (LEAP) tomograph (LEAP5000 XS; CAMECA Instruments). The field evaporation of the tip samples, maintained at 60 K, were performed at 40-pJ laser energy and 250-kHz frequency, and at least 5 million ions were acquired for each of the measurements. Data reconstruction and analysis were performed using IVAS software provided by CAMECA. Boron quantification was off in the measurements and corrected based on calibration using a MoB standard sample.

Indentation Hardness

Indentation hardness was performed on as-polished, as-printed samples of Mo-4Si-6B. A 10-kg force with Vickers indentation was used. The large force during hardness testing was evaluated to gauge the samples' resistance to cracking under the high load.

RESULTS

Design of Experiments Using a Dimensionless Number

A dimensionless number is usually expressed by a group of parameters, related to the process as well as inherent to the material, and can be utilized to study AM processes.[24,25] Recently, a dimensionless number has been developed for the DED system as a function of process parameters such as laser power P, laser spot diameter D_l, feed rate v (laser traverse speed), layer thickness Z, hatch spacing h, and mass flow rate $\dot{m}$, as well as materials properties, such as thermal diffusivity α, specific heat capacity C_p, latent heat of fusion H_f, and melting point T_m. The Buckingham PI theorem[26] was used to derive a relationship between the process parameters, machine parameters, and properties of interest. The details of the dimensionless number can be found elsewhere,[20] but are summarized for clarity. A primary assumption in the analysis is that the process parameters are a strong function of the global energy density ($E_g = P/vD_l$) into the system, the thermal diffusivity ($\alpha = k/\rho C_p$), the mass flow rate ($\dot{m}$), and the latent heat of fusion and sensible heat ($H = H_f + C_p \times (T_m - T_o)$).

Using the Buckingham PI theorem in Eq. 2, the dimensionless number was derived as:[20]

$$\Pi_1 = \frac{E_g \times \alpha}{\dot{m} \times H} \tag{2}$$

In a DED system, properties such as density and build height are also influenced by hatch spacing (h) and layer thickness (Z). Thus, a dimensionless length $L^* = Z/h$ is introduced in Eq. 3, and the dimensionless number can be expressed as:

$$\Pi_2 = \frac{E_g \times \alpha}{\dot{m} \times H} \times \frac{Z}{h} \quad (3)$$

Both layer thickness and hatch spacing can be correlated to the laser spot size (D_l) to avoid porosities such as lack-of-fusion and keyholes in the printed components. Using the physical properties of the premixed powder, the temperature distribution can be approximated from the Rosenthal equation.[27] Thus, both layer thickness (Z) and hatch spacing (h) can be correlated with laser spot diameter, D_l, as follows: $Z \leq 0.4 \sim 0.8D_l$ and hatch spacing, $h \leq 0.5 \sim 0.6D_l$. A normalized build height has been defined as:

$$h^* = \frac{h_{\text{actutal}}}{(n \times Z) \times \dot{m}} \quad (4)$$

where h^*, h_{actual}, n, Z, and $\dot{m}$ are the normalized build height, actual build height, number of layers printed, layer thickness, and mass flow rate, respectively. As an initial effort, process parameters have been estimated from Ref. 20 where a linear correlation between build height and the dimensionless number was defined as:

$$h^* = 2 \times 10^{-3} \times \Pi_2 \quad (5)$$

The normalized height increases with the dimensionless number due to the increase in input power. The linear correlation was further used to predict the print parameters with controlled flow rates. For example, a consistent build in the DED process requires that the actual build height needs to match the Z increment of the laser head with respect to the sample surface. In other words, the focal spot distance of the laser (stand-off distance) should be kept constant for a consistent build at each layer. Therefore, at a mass flow rate of 5.5 g/min, if $\frac{h_{\text{actutal}}}{n \times Z}$ is set to 0.9∼1.0 to maintain dimensional accuracy, and a layer thickness and hatch spacing of 0.254 mm is used in Eq. 5, the predicted power will lie within the range of 600∼750 W at a feed rate of 6.3 mm/s. With this predicted narrow window, the parameters were expanded to verify this process window analysis. The range of process parameters was chosen within $20 < \Pi_2 < 213$. The printing process parameters for the reactive synthesis of Mo-Si-B alloy used in this study are listed in Table I.

High-Throughput Synthesis

Process parameters for the reactive synthesis of the Mo-Si-B alloy were defined using Eq. 5, as shown in Table I. Using these process parameters, 25 Mo-Si-B bulk samples (with the nominal composition of Mo-4Si-6B) were printed at different dimensionless numbers on a titanium build plate with premixed Mo, Si_3N_4, and BN powder. The samples were collectively ground and polished to present a representative cross-section of the material. The placement and the adherence of the samples on the build plate is demonstrated in Fig. 3a. Not all samples were of equal build quality because of the wide range of process parameters used.

To validate the predicted process window from Eq. 5, the build height of each sample was measured and plotted with respect to the dimensionless number, Π_2 (Fig. 3b). Different flow rates of powder are shown with different colors on the plot. A subset of the samples followed the predicted trend line, and most of the samples were produced with a flow rate of 5.5 g/min and a few samples with the highest flow rate of 11 g/min. No samples with the lower flow rates of 2 and 3.1 g/min followed the predicted relationship, and adherence to the predicted range in Eq. 5 only occurred between $50 < \Pi_2 < 100$. This range is marked with the red dashed oval in Fig. 3b and should be considered as a transition boundary to lower-quality builds. The samples with lower flow rates of powder, even with higher energy density inputs, did not build to the same height level as the samples with higher flow rates. In general, the predictive relationship only worked in the specific range of the wide parameter set investigated.

Microstructural Characterization

To evaluate the quality of the printed samples, porosity and cracks in them were investigated using SEM and are shown in Fig. 4b–f. An SEM micrograph of four different samples taken from four different dimensionless numbers are shown. The data are plotted in a different way in Fig. 4a to allow comparison to Fig. 3b. In the DED process, the build height should optimally match the Z increment (programmed layer thickness) to maintain a constant stand-off distance. If the build height is less or more than the Z increment, the laser will be out of focus and result in an ineffective build. Build height can be systematically controlled and investigated by varying the laser input power (P), feed rate (v), and

Table I. Process parameter ranges for the reactive synthesis of Mo-Si-B refractory metal alloy

Power (W)	Feed rate (mm/s)	Hatch spacing (mm)	Layer thickness (mm)	Mass flow rate (g/min)
400–800	6.3–10.6	0.254	0.254	2∼11
Optimum process parameters				
600	6.3	0.254	0.254	5.5

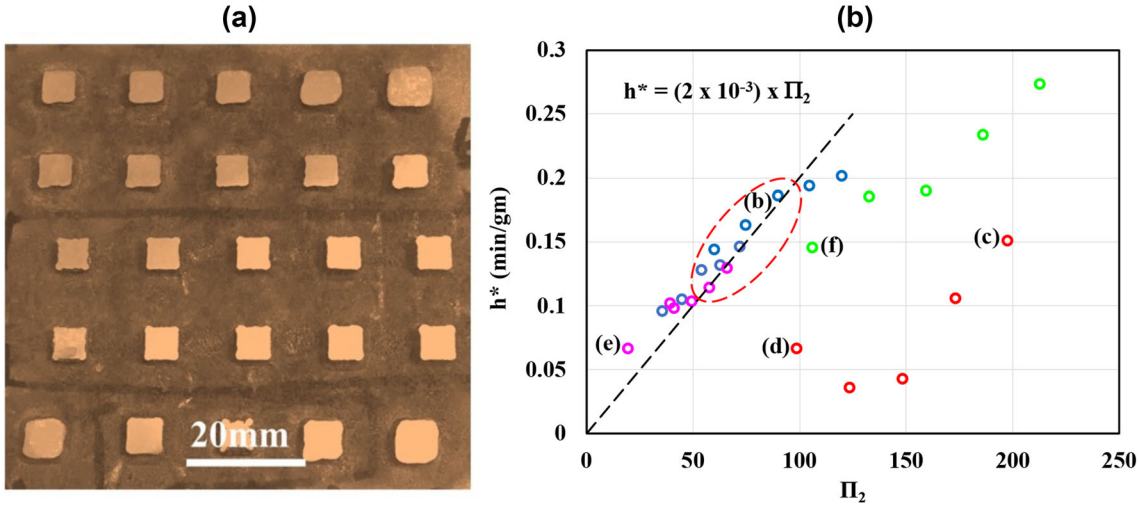

Fig. 3. (a) A titanium build plate with 25 Mo-Si-B samples, and (b) the relationship between normalized height and dimensionless number. The different colored data represent different flow rates, where red is 2 g/min, green is 3.1 g/min, blue is 5.5 g/min, and pink is 11 g/min. Different samples are labeled which will be presented with microstructural analysis (Color figure online).

mass flow rate ($\dot{m}$) while keeping the layer thickness (Z) and hatch spacing (h) constant. An increase in input power and mass flow rate is anticipated to result in an increase in build height when the feed rate remains constant. However, when the input power and mass flow rate remain constant, a higher feed rate is likely to result in a reduction of the build height.

Thus, to investigate the effect of process parameters on the build height, a normalized build height (h/h_{set}) as a function of $[(P \times \dot{m})/v]$ has been plotted (Fig. 4a), in which, four data points, (c–f), correspond to both low $[(P \times \dot{m})/v]$ and h/h_{set} values. Specifically, data points (c–f) correspond to $((P \times \dot{m})/v) < 7.5$ and $h/h_{set} < 0.75$. Sample (e) had a low Π_2, while samples (c), (d), and (f) had higher Π_2 values. The samples are labeled consistently between Figs. 3b and 4a to permit comparison. Sample (b) had a h/h_{set} near 1 and a $\Pi_2 = 90$, and is the optimal print parameter setting predicted and defined in Table I.

All four samples (c–f) exhibited varying levels of porosity defects. These samples did not fall on the predicted relationship line for normalized build height, and this fact is more clearly demonstrated with the replotting of the data in Fig. 4a, where all four samples did not build at a rate required to keep the laser beam in focus. For example, porosities in 3D printing are processing defects that may occur during metal additive AM at high input energy densities. A sample at a high dimensionless number, i.e., $\Pi_2 = 200$, containing this type of defect is shown in Fig. 4c. In this case, the laser input energy was relatively high (800 W), and the mass flow rate was lower (2 g/min) than the pore-free optimized sample shown in Fig. 4b. Another sample taken at a low $P \times \dot{m}/v$ ($\Pi_2 = 20$) is shown by the data point (d) in Fig. 4a. This sample exhibits porosity defects with a reasonable Π_2 (99) value that is not on the predicted relationship line given by Eq. 5. The sample had a low power ($P = 400$ W) at a higher feed rate, i.e., 10.6 mm/s, and a lower mass flow rate of 2 g/min.

Another sample at a low $[(P \times \dot{m})/v]$, unmelted powder (in this case molybdenum) can be found in the sample shown in Fig. 4e. This sample also falls outside the optimum process parameter window and was made with a laser power of 400 W, a feed rate of 10.6 mm/s, and a mass flow rate of 10 g/min. The laser input energy was lower and the feed rate was higher compared to the predicted optimized sample (Fig. 4b). Due to the insufficient amount of energy available for the melting of the powders, the final print exhibited unmelted powder and a lack of bonding. Finally, sample (f) has a higher Π_2 (= 106) but still a lower $[(P \times \dot{m})/v]$. This sample also had significant cracking, and the cracks may be a result of insufficient energy for bonding. These results suggest that, while adherence to the relationship stated in Eq. 5 is necessary, it is also important for the actual build height to increase at the same level as the Z increment during the build process. The build height assessment offers further process parameter prediction and optimization in addition to the relationship in Eq. 5.

The sample with the optimum predicted process parameter, i.e., at $\Pi_2 = 90$, is shown in Fig. 4b. The laser power, scan speed, and powder flow rate were 600 W, 6.3 mm/s, and 5.5 g/min, as listed in Table I. A large area SEM scan of this sample indicates no visible cracks or defects (see Figs. 4b and 5a–d. Within this optimum region, the process parameters were obtained from Eq. 5. A relatively high-magnification micrograph of this sample is shown in Fig. 5b–d where inter-dendritic regions are visible. Both primary dendritic arm spacing (PDAS) and secondary dendritic arm spacing (SDAS) are visible in Fig. 5c (white and cyan colored dotted arrow).

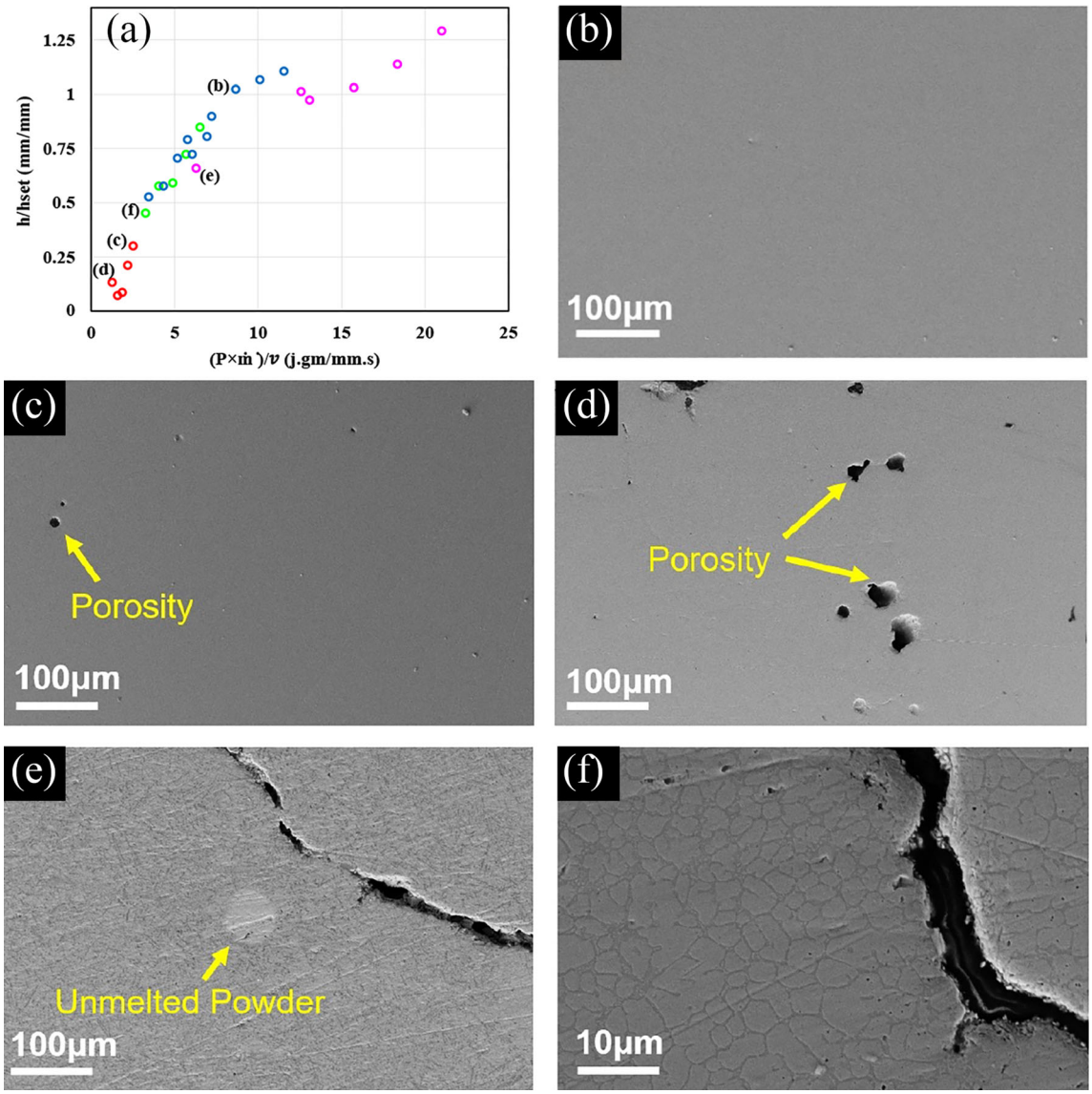

Fig. 4. Microstructural investigation of printed samples: (a) build height as a function of laser power, mass flow rate, and feed rate, (b) defect-free sample printed with optimum process parameters, (c) small pores in printed sample, (d) sample with large pores, (e) sample with unmelted powder and lack of bonding due to insufficient amount of energy input, and (f) a sample with extensive cracks.

The PDAS is on the order of 5 μm while the SDAS is $\sim$ 1 μm. In addition, a higher magnification SEM micrograph reveals the existence of the T2 phase in the sample as shown by the red dotted arrow in Fig. 5d. At a higher magnification, both a Mo_{ss} matrix and the T2 phases can be found in the as-printed sample.

To confirm the complete chemical reaction during this reactive synthesis during manufacturing, an APT study was conducted by following the procedure mentioned in "Materials and Methods" section. The backscattered SEM micrograph of a sample at $\Pi_2 = 90$ is shown in Fig. 5e, where the Mo-rich phase (dense; bright) and the T2 phase (dark contrast) are observed. No cracks, pores, or inclusions can be seen. The 3D elemental distributions of the printed samples by APT are shown in Fig. 5f and g. A homogeneous distribution of Mo and Si elements with negligible impurities is observed for the Mo-Si-B ($Mo_{90}Si_4B_6$ at.% nominal composition) sample, demonstrating superior build quality and complete mixing during this reactive synthesis process. The Mo-rich matrix exhibited a composition of $\sim Mo_{98}Si_2$, which indicates a Si supersaturation, and an insignificant solubility of B was observed. A homogenous distribution of elements even at the phase boundaries is observed, further indicating the high quality of the build possible using reactive synthesis in the AM technique.

Indentation Hardness

Although Vickers hardness testing is not a rigorous substitute for tensile strength or ductility, the tests can provide a relative insight into these

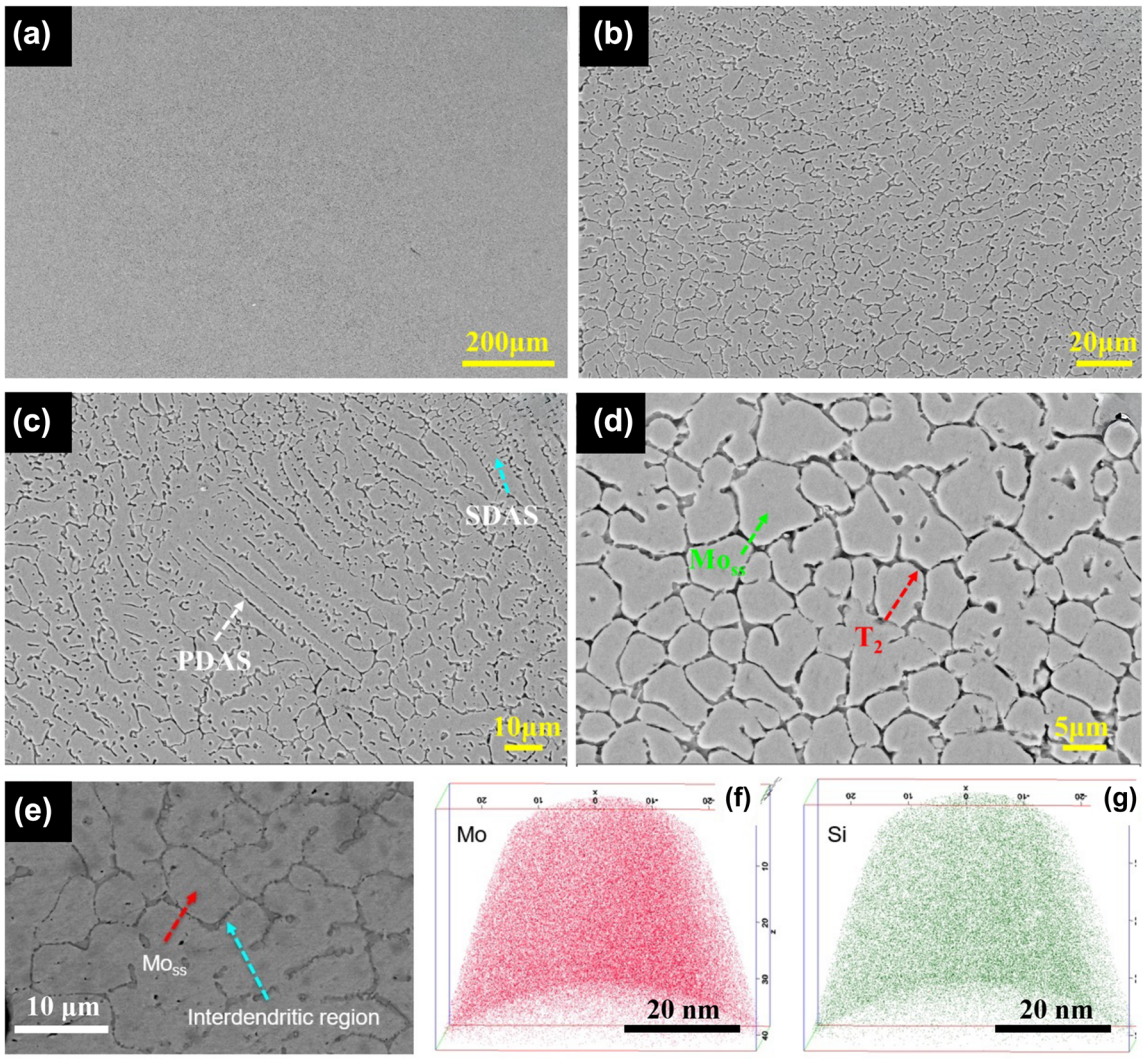

Fig. 5. (a–d) SEM micrograph of Mo-Si-B alloy sample printed at optimum process conditions shown at different magnifications, (e) Backscattered SEM micrograph: (f) and (g) 3D elemental distribution of Mo and Si, respectively, inside the matrix captured by APT (Color figure online).

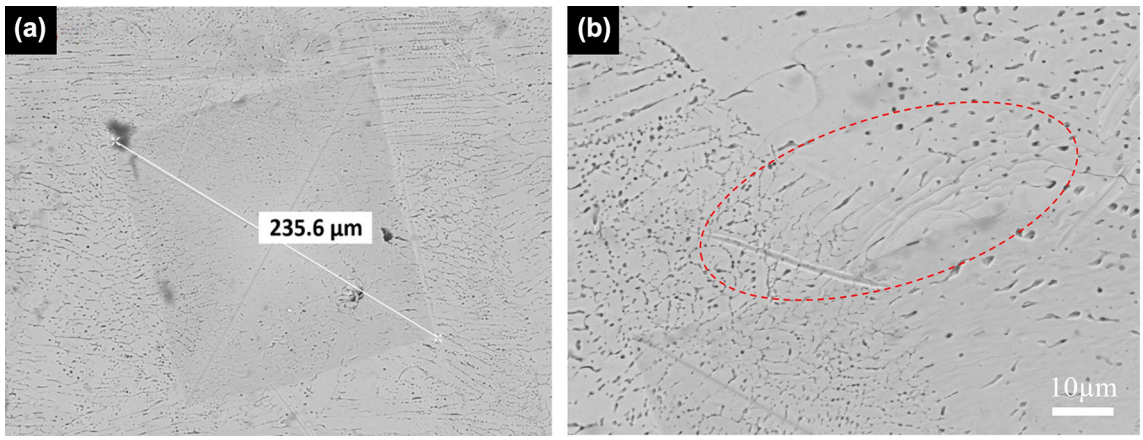

Fig. 6. Vickers hardness with a 10-kg force on the as-printed Mo-4Si-6B samples, where (a) shows the full indent with the diagonal length marked and (b) demonstrates plastic flow lines on the side (circled) of an indent.

mechanical properties. Micrographs of the indented samples are shown in Fig. 6a and b. Indeed, the high load indent indicates no cracking with plastic slip lines evident in the sample. The HV10 hardness values was 314.5, suggesting a material with high strength values.

DISCUSSION

Metal AM offers a viable methodology to fabricate complex, near-net-shape refractory Mo-based components with high density. Conventional processing of refractory components with high density is a technical challenge because of the high-temperature requirements. For example, conventional casting methods introduce containment challenges because the melting temperatures of the refractory alloys are near that of ceramic crucibles. Powder metallurgy methods require additional consolidation methods at energy-intensive (and expensive) processing temperatures. In addition, the sluggish diffusion kinetics require longer times for chemical homogenization. With metal AM, the high energy density within the focal spot size of the laser beam alloys permits the melting of the ultrahigh melting temperature metals. During solidification, chemical homogenization times are reduced because of the refined microsegregation distances associated with high cooling rates in the process.[28] The biggest challenge in metal AM of new materials is predicting the required process parameters.

The use of a dimensionless number allows a design of an experimental matrix to be produced to predict and optimize the required process parameters. The dimensionless number, which reflects a ratio of the heat input (for melting a volume of an alloy) to the heat extraction, is further optimized when the actual build height of each layer is nearly equivalent to the Z increment programmed as the step height for each layer. Porosity defects and cracking are eliminated with the proper processing conditions, even when a pre-blended mixture of powder is used. Although the dimensionless number was originally validated on Fe-based materials, the extension of the method to other materials such as the refractory Mo alloy is possible.

Pre-blending of powder offers potential cost reductions for refractory components or sample fabrication. The use of elemental Mo along with Si_3N_4 and BN allows for additional alloying investigations, as well as compositional grading with feedstock that is readily available and not requiring special orders for commercial suppliers. Also, the reactive synthesis of the Mo powder with Si_3N_4 and BN provides additional heat to assist with the processing without retaining nitrogen in the sample. No evidence of unmelted nitride powder was observed, and no nitrogen was detected in the samples. The final two-phase microstructures (Mo_{ss} + T2) resulted from the reactive synthesis during DED processing. Dendrite arm spacings were on the order of 1–5 μm, with the SDAS of $\sim$ 1 μm being consistent with the high cooling rates found in DED processing of steels. The microsegregation resulted in T2 residing in the interdendritic region, so chemical homogenization may not be required for chemical uniformity. However, supersaturation in the Mo_{ss} may require heat treatment for precipitation and further enhancement of potential ductility in the matrix.

Despite the potential for a slightly supersaturated Mo_{ss} in the as-printed samples, the indented samples exhibited slip lines, indicating the sample's ability to plastically deform, even with high Vickers hardness loads. Future studies will focus on extending the concepts to different alloys, tensile testing, and scaling the DED processing to other AM techniques using the dimensional analysis.

CONCLUSION

The present study aimed to fabricate new refractory alloys with metal AM. To potentially facilitate the processing, reactive synthesis was used by reacting Mo with ceramic nitride powders. The design process parameters for the new material were based on a previously developed relationship between measured height and dimensionless number using process parameters as well as thermophysical properties. The following are the conclusions of this present study:

1. Reactive synthesis of Mo with nitride powders was used during DED processing to produce chemically uniform samples.
2. Process parameters for full density AM of a refractory MoSiB alloy were predicted by using a dimensionless number previously developed for Fe-based alloys.
3. Microstructural investigations indicate that, within the optimum process window, porosity-free samples can be printed with dimensional accuracy, uniform microstructures, and refined microsegregation (1–5 μm), particularly when the actual build height is the same as the programmed layer height.
4. The chemical composition obtained from the APT study confirms the reactive synthesis process between the alloying powders during the DED-based reactive manufacturing of the Mo-Si-B alloy with negligible impurities.
5. Vickers indentation with a 10-kg force indicates appreciable strength (314 HV10) with observable plastic slip traces.

ACKNOWLEDGEMENTS

The authors would like to gratefully acknowledge the support of the Department of Energy (DOE), Advanced Research Projects Agency-Energy (ARPA-E) Ultrahigh Temperature Impervious Materials Advancing Turbine Efficiency (ULTIMATE) Program (DE-AROOO1431). APT was performed at the

Northwestern University Center for Atom-Probe Tomography (NUCAPT). The LEAP tomograph at NUCAPT was purchased and upgraded with grants from the NSF-MRI (DMR-0420532) and ONR-DURIP (N00014-0400798, N00014-0610539, N00014-0910781, N00014-1712870) programs. NUCAPT received support from the MRSEC program (NSF DMR-1720139) at the Materials Research Center, the SHyNE Resource (NSF ECCS-2025633), and the Initiative for Sustainability and Energy (ISEN) at NU.

CONFLICT OF INTEREST

On behalf of all authors, the corresponding author states that there is no conflict of interest.

REFERENCES

1. J.H. Perepezko and R. Sakidja, *Adv. Eng. Mater.* 11, 892 https://doi.org/10.1002/adem.200900118 (2009).
2. J.H. Perepezko, *Science* 326, 1068 https://doi.org/10.1126/science.1179327 (2009).
3. D.M. Dimiduk and J.H. Perepezko, *MRS Bull.* 28, 639 https://doi.org/10.1557/mrs2003.191 (2011).
4. L. Su, O. Lu-Steffes, H. Zhang, and J.H. Perepezko, *Appl. Surf. Sci.* 337, 38 https://doi.org/10.1016/j.apsusc.2015.02.061 (2015).
5. D.R. Lide, *Crc Handbook of Chemistry and Physics 2008–2009: A Ready-Reference Book of Chemical and Physical Data* (CRC Press-Taylor & Francis, Cleveland, 2008).
6. M. Krüger, S. Franz, H. Saage, M. Heilmaier, J.H. Schneibel, P. Jéhanno, M. Böning, and H. Kestler, *Intermetallics* 16, 933 https://doi.org/10.1016/j.intermet.2008.04.015 (2008).
7. J.L. Yu, Z.K. Li, X. Zheng, J.J. Zhang, H. Liu, R. Bai, and H. Wang, *Mater. Sci. Eng. A* 532, 392 https://doi.org/10.1016/j.msea.2011.11.001 (2012).
8. J.A. Shields Jr. and E.L. Baker, *Adv. Mater. Processes* 155, 61 (1999).
9. J.J. Kruzic, J.H. Schneibel, and R.O. Ritchie, *Metall. Mater. Trans. A* 36, 2393–2402 https://doi.org/10.1007/s11661-005-0112-5 (2005).
10. J.H. Perepezko and R. Sakidja, *JOM* 62, 13 https://doi.org/10.1007/s11837-010-0148-x (2010).
11. P. Ritt, R. Sakidja, and J.H. Perepezko, *Surf. Coat. Technol.* 206(19–20), 4166 https://doi.org/10.1016/j.surfcoat.2012.04.016 (2012).
12. P. Jain and K.S. Kumar, *Scr. Mater.* 62, 1 https://doi.org/10.1016/j.scriptamat.2009.09.008 (2010).
13. D. Sturm, M. Heilmaier, J.H. Schneibel, P. Jéhanno, B. Skrotzki, and H. Saage, *Mater. Sci. Eng. A* 463, 107 https://doi.org/10.1016/j.msea.2006.07.153 (2007).
14. M.K. Miller, E.A. Kenik, M.S. Mousa, K.F. Russell, and A.J. Bryhan, *Scr. Mater.* 46, 299 https://doi.org/10.1016/S1359-6462(01)01242-8 (2002).
15. M.K. Miller and A.J. Bryhan, *Mater. Sci. Eng. A* 327, 80 https://doi.org/10.1016/S0921-5093(01)01880-9 (2002).
16. H. Saage, M. Krüger, D. Sturm, M. Heilmaier, J.H. Schneibel, E. George, L. Heatherly, C. Somsen, G. Eggeler, and Y. Yang, *Acta Mater.* 57, 3895 https://doi.org/10.1016/j.actamat.2009.04.040 (2009).
17. L. Liu, C. Shi, C. Zhang, P.M. Voyles, J.H. Fournelle, and J.H. Perepezko, *Intermetallics* 116, 106618 https://doi.org/10.1016/j.intermet.2019.106618 (2020).
18. X. Nan, S. Ida, N. Sekido, K. Yoshimi, and J.H. Perepezko, *Corros. Sci.* 214, 110990 https://doi.org/10.1016/j.corsci.2023.110990 (2023).
19. B. Barroqueiro, A. Andrade-Campos, R. Valente, and V. Neto, *J. Manuf. Mater. Process.* 3, 52 (2019).
20. Z. Islam, P. Nelaturu, and D.J. Thoma, *Appl. Phys. Lett.* 119, 231901 https://doi.org/10.1063/5.0069384 (2021).
21. M.R. Middlemas and J.K. Cochran, *JOM* 60, 19 https://doi.org/10.1007/s11837-008-0084-1 (2008).
22. D. Pu and Y. Pan, *Vacuum* 196, 110727 https://doi.org/10.1016/j.vacuum.2021.110727 (2022).
23. W. Cao, S.L. Chen, F. Zhang, K. Wu, Y. Yang, Y.A. Chang, R. Schmid-Fetzer, and W.A. Oates, *Calphad* 33, 328 https://doi.org/10.1016/j.calphad.2008.08.004 (2009).
24. M. van Elsen, F. Al-Bender, and J.P. Kruth, *Rapid Prototyp. J.* 14, 15 https://doi.org/10.1108/13552540810841526 (2008).
25. T. Mukherjee, V. Manvatkar, A. De, and T. DebRoy, *J. Appl. Phys.* 121, 064904 https://doi.org/10.1063/1.4976006 (2017).
26. E. Buckingham, *Phys. Rev.* 4, 345 https://doi.org/10.1103/PhysRev.4.345 (1914).
27. D. Rosenthal, *Trans. Am. Soc. Mech. Eng.* 68, 849 https://doi.org/10.1115/1.4018624 (2022).
28. K.M. Bertsch, G.M. De Bellefon, B. Kuehl, and D.J. Thoma, *Acta Materialia*, 199, 19 https://doi.org/10.1016/j.actamat.2020.07.063 (2020).